

Evidence for Solar-Wind Charge-Exchange X-Ray Emission from the Earth's Magnetosheath

Ryuichi FUJIMOTO¹, Kazuhisa MITSUDA¹, Dan MCCAMMON², Yoh TAKEI¹, Michael BAUER³,
Yoshitaka ISHISAKI⁴, F. Scott PORTER⁵, Hiroya YAMAGUCHI⁶, Kiyoshi HAYASHIDA⁷, and Noriko Y. YAMASAKI¹

¹*ISAS/JAXA, 3-1-1 Yoshinodai, Sagamihara 229-8510
fujimoto@astro.isas.jaxa.jp*

²*University of Wisconsin, Madison, WI 53706, USA*

³*Max-Planck-Institut für extraterrestrische Physik, D-85740 Garching, Germany*

⁴*Tokyo Metropolitan University, 1-1 Minami-Osawa, Hachioji, Tokyo 192-0397*

⁵*NASA Goddard Space Flight Center, Greenbelt, MD 20771, USA*

⁶*Department of Physics, Faculty of Science, Kyoto University, Sakyo-ku, Kyoto 606-8502*

⁷*Department of Astrophysics, Faculty of Science, Osaka University, Toyonaka 560-0043*

(Received 2006 July 26; accepted 2006 September 9)

Abstract

We report an apparent detection of the C VI $4p$ to $1s$ transition line at 459 eV, during a long-term enhancement (LTE) in the *Suzaku* north ecliptic pole (NEP) observation of 2005 September 2. The observed intensity of the line is comparable to that of the C VI $2p$ to $1s$ line at 367 eV. This is strong evidence for the charge-exchange process. In addition to the C VI lines, emission lines from O VII, O VIII, Ne X, and Mg XI lines showed clear enhancements. There are also features in the 750 to 900 eV range that could be due to some combination of Fe XVII and XVIII L-lines, higher order transitions of O VIII ($3p$ to $1s$ and $6p$ to $1s$), and a Ne IX line. From the correlation of the X-ray intensity with solar-wind flux on time scales of about half a day, and from the short-term (~ 10 minutes) variations of the X-ray intensity, these lines most likely arise from solar-wind heavy ions interacting with neutral material in the Earth's magnetosheath. A hard power-law component is also necessary to explain the LTE spectrum. The origin of this component is not yet known. Our results indicate that solar activity can significantly contaminate *Suzaku* cosmic X-ray spectra below ~ 1 keV. Recommendations are provided for recognizing such contamination in observations of extended sources.

Key words: atomic processes — Sun: solar wind — Earth — interplanetary medium — X-rays: diffuse background

1. Introduction

Snowden et al. (1994) reported the existence of mysterious X-ray contamination episodes in the *ROSAT* all sky survey data which they termed long-term enhancements (LTEs). During an LTE, the X-ray counting rate in the lower energy bands as much as doubled on a time scale of 1–2 days. However, they could not find any correlation with other observational parameters, such as spacecraft position or look direction. New insight on LTEs was obtained by the discovery of X-ray emission from comet Hyakutake (Lisse et al. 1996). Following the discovery, X-rays were detected from many comets (e.g., Dennerl et al. 1997; Cravens 2002), and the emission mechanism is now well understood as charge exchange of solar-wind heavy ions with cometary neutrals (see Krasnopolsky et al. 2004 for a review). Then Cox (1998) and Cravens (2000) suggested that solar-wind charge exchange with neutrals in the Earth's geocorona and in the heliosphere accounts for a part of soft X-ray background below 1 keV. Robertson et al. (2001) showed that the LTEs of the *ROSAT* all sky survey data were well cor-

related with the solar-wind proton flux, which strongly suggests the origin of the LTEs to be solar-wind charge exchange with HI in the geocorona. Solar-wind charge exchange results in line emission from highly ionized ions (Krasnopolsky et al. 2004 and references therein). *ROSAT* did not have enough spectral resolution to resolve those lines. Spectral information on geocoronal solar-wind charge exchange was first obtained during a *Chandra* dark moon observation (Wargelin et al. 2004). The X-ray photons detected in the direction of the dark moon are most likely from this source. The emission spectrum could be described by a sum of C VI, O VII, and O VIII K-lines, although the statistics and energy resolution were limited. More recently, Snowden, Collier, Kuntz (2004) reported time variation of soft X-ray intensity during the *XMM-Newton Hubble* deep field north observation. The enhancement was correlated with solar-wind proton flux variations. They detected C VI, O VII, O VIII, Ne IX, and Mg XI emission lines in the enhancement.

The importance of solar-wind charge-exchange emission is three-fold. Firstly, it will enable us to remotely study low density neutrals in geocorona, in outer atmosphere of

planets such as Jupiter, in interplanetary space, and in particular, around comets. Secondly, it can be used as a highly sensitive ion probe for the solar wind. Perhaps most importantly, it becomes a significant contaminating foreground in the study of the cosmic soft X-ray background below ~ 1 keV. More than half of the soft X-ray background at these energies is considered to arise from hot gas in the disk and halo of our galaxy and in intergalactic space. Although such emission was detected early in the history of X-ray astronomy (e.g. Tanaka, Bleeker 1977), its origins and the physical state of the hot gas are not yet well understood. Geocoronal interactions with the solar wind produce at least a sporadic contamination that must be avoided in observations of any extended source. Charge exchange with interstellar neutrals moving through the heliosphere creates a more subtle contribution where much of the diagnostic rapid time variation is washed out by the large travel time of solar-wind events through interplanetary space, and the spectral lines arise from the same ions expected in hot interstellar plasmas. Lallement (2004) used a simplified model of interplanetary charge exchange to estimate that essentially all of the minimum flux observed near the Galactic plane in the 1/4 keV (R12) band of the *ROSAT* sky survey could arise from this source (see also Pepino et al. 2004). We are far from an understanding of solar-wind charge exchange adequate to determine the true extent of this contribution.

The X-ray Imaging Spectrometer (XIS) on board *Suzaku* (Mitsuda et al. 2006) has a significantly improved spectral line response function compared to previous X-ray CCD cameras, particularly below 1 keV (Koyama et al. 2006). Together with the large effective area of the X-ray telescopes (XRT; Serlemitsos et al. 2006), this will open a new era for the study of soft X-ray background. In this paper, we report on *Suzaku* observations of a blank field in direction of the north ecliptic pole (NEP). We detected a significant enhancement of the soft X-ray flux lasting for ~ 10 hours. The enhancement is mostly explained by increases in C VI through Mg XI emission lines. During the enhancement, both C VI $n = 2$ to 1 and C VI $n = 4$ to 1 transition lines were clearly detected, which is a firm evidence for charge-exchange emission. We consider that the emission is due to the charge-exchange interaction of solar-wind heavy ions with neutrals in the magnetosheath at 2–8 Earth radii (R_{\oplus}). In this paper, we will concentrate on the X-ray spectra and the emission processes, and their implications for cosmic X-ray observations. The geophysical implications of the results will be discussed in a separate paper.

Errors quoted in the text and tables are at 90% confidence single parameter errors and at 1σ confidence level in the figures, unless otherwise stated.

2. Analysis and results

The NEP region was observed with *Suzaku* twice during the Science Working Group (SWG) observation time. The XIS was set to normal clocking mode and the data format was either 3×3 or 5×5 . A log of the observations is shown

in table 1. In this paper, we concentrate on the spectral change during a “flare” detected in the first observation. For that purpose, we try to model the stable components, and then evaluate the spectral change. We use the data from the backside-illuminated CCD (XIS1), because of its much superior performance below 1 keV (Koyama et al. 2006).

2.1. Data reduction

We used version 0.6 processed *Suzaku* data¹. In addition to the standard data selection criteria: elevation from sunlit earth rim $> 20^\circ$, elevation from dark earth rim $> 5^\circ$, we applied cutoff rigidity (COR) > 8 to clean the XIS data. The XIS pulse height data for each X-ray event (3×3 or 5×5 format) were converted to PI (Pulse Invariant) channels using the ‘xispi’ software version 2005-12-26 and CTI parameters from 2006-01-25.

We first created a time history of the X-ray counting rate by binning the event data into 256 s time bins. In figure 1, we show the 0.3–2 keV counting rate of XIS1 where the non-X-ray (particle-induced) background rate is not subtracted. The counting rate shows a clear enhancement in the first $\sim 4 \times 10^4$ s. The particle background rate of the XIS is known to vary because the cosmic ray flux changes as a function of the spacecraft position over the Earth. The background rate is well reproduced as a consistent function of the local cutoff rigidity. From the XIS data during intervals when the telescope is pointed at the dark side of the Earth, we found that the 0.3–2 keV XIS1 non-X-ray counting rate varies only from 0.03 ctss^{-1} to 0.07 ctss^{-1} when the cutoff rigidity varies from 15 to 6 GV. Thus the observed enhancement cannot be particle background variation.

The enhancement lasted for ~ 10 hours. Within the enhancement there are shorter time variations. For example, there are sharp spikes just before and after the highest peak at $\sim 2.2 \times 10^4$ s. A time scale of these variations is as short as ~ 10 minutes. We defined the “flare” interval to be 0 to 4×10^4 s and the “stable” interval as 4×10^4 to 16.5×10^4 s as shown in figure 1, then created X-ray images for “flare” and “stable” periods separately. The images in figure 2 show that the enhancement is not due to changes in any discrete sources.

We subtracted the particle background from both “sta-

¹ Version 0 processing is an internal processing applied to the *Suzaku* data obtained during the SWG phase, for the purpose of establishing the detector calibration as quickly as possible. Some processes that are not critical for most of the initial calibration and scientific studies, e.g., aspect correction, fine tuning of the event time tagging of the XIS data, are skipped in version 0 processing, and hence, quality of the products is limited in these directions, compared with the official data supplied to the guest observers. As of 2006 July, version 0.7 is the latest, where the absolute energy scale accuracy of ± 0.2 eV at the iron $K\alpha$ energy and ± 5 eV below 1 keV is achieved for the XIS data (Koyama et al. 2006). In this paper, we used version 0.6 data where the energy scale of the XIS data are less accurate (~ 10 eV below 1 keV) than that of version 0.7, because the empirical model of the contamination distribution was obtained based on version 0.6 data. Instead, we adjusted the scale and the offset of the response matrix, as shown in section 2.1.

Table 1. Log of the NEP observations

| target coordinates | $(\alpha, \delta) = (272.8000, 66.0000)$ | |
|--------------------|--|--|
| observation ID | 100018010 | 500026010 |
| observation period | 2005 Sep. 2 14:30–Sep. 4 15:00 | 2006 Feb. 10 5:50–Feb. 12. 2:00 |
| net exposure time | 109.8 ks | 88.6 ks |
| | $(3 \times 3: 95.7 \text{ ks}, 5 \times 5: 14.1 \text{ ks})$ | $(3 \times 3: 71.5 \text{ ks}, 5 \times 5: 17.1 \text{ ks})$ |

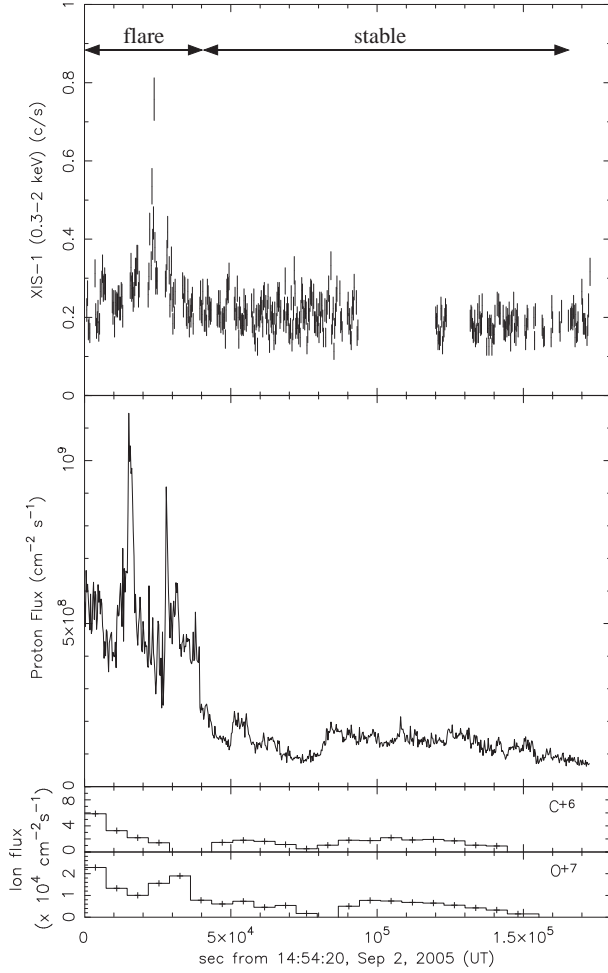


Fig. 1. XIS1 counting rate in the 0.3–2 keV energy band (top panel), solar-wind proton flux (second), C^{+6} flux (third), and O^{+7} flux (bottom) as a function of time. The *Suzaku* XIS counting rate is shown in 256 s bins. Particle background counts are not subtracted. The solar-wind proton flux was calculated using level 2 ACE SWEPAM data. Each bin of the ACE data was first shifted in time to correct for the travel time of the solar wind from ACE to the Earth (typically ~ 2700 s), then rebinned into 256 s bins. The ion fluxes (C^{+6} , O^{+7}) were calculated from level 2 ACE SWICS data. Only good data with quality flag 0 were used. See also text in section 3.

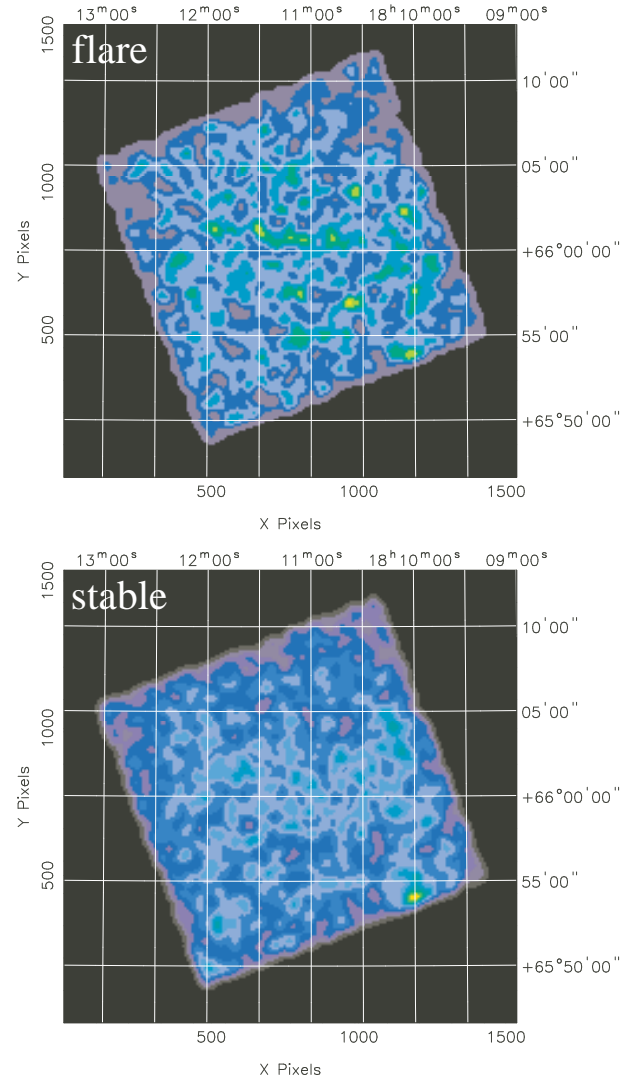


Fig. 2. XIS1 images in the 0.3–2 keV band for “flare” and “stable” periods.

ble” and “flare” spectra using the dark earth data with the same distribution of cutoff rigidities. The counting rates of the background subtracted spectra above 10 keV, where the data are dominated by non X-ray background events, are $(2.9 \pm 0.5) \times 10^{-2}$ cts s^{-1} for “flare” and $(1.2 \pm 0.3) \times 10^{-2}$ cts s^{-1} for “stable”, where the error is 1σ statistical error. These correspond to 6% and 2% of the counting rates of the dark earth data, respectively. Note that, in the 2–5 keV band, change of the spectral model due to this background difference is much smaller than the statistical error, and hence, they do not affect the results in the later sections.

Since we suppose the diffuse X-ray emission to be approximately uniform over the field of view of the XIS, we created an X-ray telescope (XRT) response function, or more specifically, an ancillary response file (ARF) used in the XSPEC spectral fit software (Arnaud 1996), for a flat field, using the XIS ARF builder software *xissimarfgen* (Ishisaki et al. 2006). It is known that contamination has been accumulating on the optical blocking filters of the XIS sensors since the detector doors were opened following the launch, and that it accumulates much more quickly at the center of the field of view than at the outside (Koyama et al. 2006). We used the contaminant thickness and radial distribution functions version 2006-05-28 when we built an ARF with *xissimarfgen*. At the early time of this NEP observation, the contaminant column densities were only 4.1×10^{17} carbon atoms cm^{-2} and 0.7×10^{17} oxygen atoms cm^{-2} at the center for XIS1. This reduces the efficiency by about 12% at the energy of C VI (367 eV), 6% at O VII (561 eV), 4% at O VIII (653 eV), and $< 2\%$ at Ne IX (905 eV) and higher energies. Systematic errors in the contaminant thickness are estimated to be about 10%. The transmission uncertainty due to this systematic error is only 1% for C VI, and less for lines at higher energies; hence it is negligible compared with other errors. For the XIS response function, we used the `ae_xi1_20060213c.rmf` file supplied by the XIS team, with energy scale corrections of slope 0.9948 and offset -0.0035 keV as determined through the iterative analysis described in the next section.

2.2. Spectral fit of “stable” spectrum

We then performed spectral fits to the “stable” spectrum. We first restricted the fitting energy range to 2–5 keV. In this range the emission is dominated by the Cosmic X-ray Background (CXB), which is largely emission from unresolved AGNs and can be represented by a power law function absorbed by neutral material along the line of sight through our Galaxy. We thus fitted the spectrum with a power-law function with absorption by a neutral medium with solar abundances (Anders, Grevesse 1989) and fixed the absorbing column density at the total Galactic value in this direction $N_{\text{H}} = 4.4 \times 10^{20}$ cm^{-2} (Dickey, Lockman 1990)². The fit results are summarized in the second column of table 2.

² We used ‘nH’ tool available at <http://heasarc.gsfc.nasa.gov/cgi-bin/Tools/w3nh/w3nh.pl>.

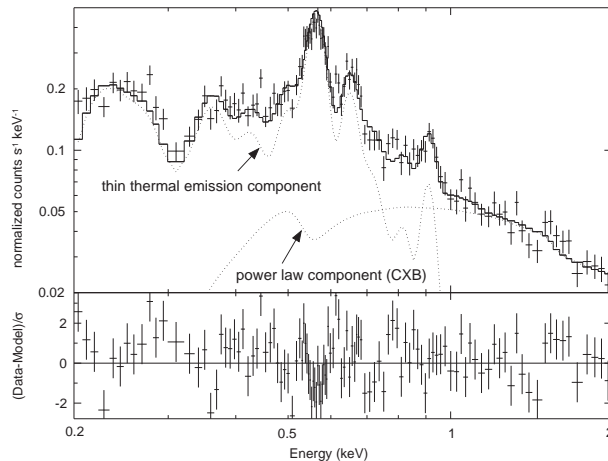


Fig. 3. Spectral fit to the “stable” spectrum in the 0.2–2 keV range. Observed spectrum is plotted in the upper panel with crosses where the vertical bars correspond to 1σ statistical errors. The thick step function is the best-fit model function convolved with the X-ray mirror and the detector response functions. The dotted lines show contributions of different spectral components. The lower panel shows the residuals of the fits.

The photon index is consistent with the nominal CXB value (1.40 ± 0.05 ; Marshall et al. 1980). The normalization of the power-law function is also consistent with previous observations; $9\text{--}11$ photons cm^{-2} s^{-1} sr^{-1} keV^{-1} at 1 keV (e.g., Gendreau et al. 1995; Revnivtsev et al. 2005).

We then fitted the spectrum over the 0.2–2 keV range. As shown in figure 3, it is clear that there is additional emission below 1 keV and the excess contains emission lines such as O VII, O VIII and Ne IX $K\alpha$. Thus, fixing the spectral parameters of the CXB component to the best fit values of the 2–5 keV fit, we added a thin thermal emission component using the MEKAL model (Mewe et al. 1985; Mewe et al. 1986; Kaastra 1992; Liedahl et al. 1995). We fixed the abundance of O at the solar value, and set abundances of other elements (C, N, Ne, Fe) free. The version 0.6 XIS data products are known to contain systematic energy calibration errors of ~ 10 eV amplitude below ~ 2 keV. We therefore adjusted the energy scale by varying the gain slope and offset as free parameters of the fit. We determined the gain and the offset in this fitting, and applied the same gain and offset throughout the paper, including the fitting of the CXB component described in the previous paragraph. The results are shown in the third column of table 2. The model adequately represent the observed spectrum³. Therefore, we adopt the model shown in table 2 as a representative model for the “stable” spectrum, in order to evaluate the spectral change during the “flare”.

The spectrum could be fit by other thermal models.

³ There are small positive residuals, especially at around 300 eV and 450 eV. We can model these features with additional delta functions of variable energy and amplitude. Even if we add them, however, normalizations of the delta functions employed for the “flare” spectrum (section 2.3) are affected by 10% at most.

Table 2. Results of spectral fits to the “stable” spectrum

| Parameter | 2–5 keV | 0.2–2 keV |
|---|----------------------|---------------------------|
| Power-law component | | |
| N_{H} [10^{22} cm $^{-2}$] | 0.044 (fixed) | 0.044 (fixed) |
| photon index Γ | 1.33 ± 0.23 | 1.33 (fixed) |
| normalization* | $10.4^{+3.1}_{-2.4}$ | 10.4 (fixed) |
| Thin-thermal component (VMEKAL) | | |
| kT [keV] | — | $0.177^{+0.003}_{-0.002}$ |
| C abundance (solar) | — | $1.92^{+0.40}_{-0.36}$ |
| N abundance (solar) | — | $2.14^{+0.33}_{-0.31}$ |
| O abundance (solar) | — | 1.0 (fixed) |
| Ne abundance (solar) | — | $2.77^{+0.53}_{-0.59}$ |
| Fe abundance (solar) | — | $1.42^{+0.20}_{-0.22}$ |
| normalization † | — | $16.35^{+0.62}_{-0.68}$ |
| gain slope | 0.9948 (fixed) | 0.9948 |
| gain offset | −0.0035 (fixed) | −0.0035 |
| $\chi^2/\text{degrees of freedom}$ | 38.39/38 | 280.15/228 |

* In units of photons cm $^{-2}$ s $^{-1}$ sr $^{-1}$ keV $^{-1}$ at 1 keV.

† $(4\pi)^{-1} D_{\text{A}}^{-2} (1+z)^{-2} 10^{-14} \int n_{\text{e}} n_{\text{H}} dV$ per steradian, where D_{A} is the angular size distance to the source (cm), and n_{e} , n_{H} are the electron and hydrogen densities (cm $^{-3}$), respectively.

When we adopt the present single temperature model with varying abundances, the temperature is determined primarily by the O VII to O VIII $K\alpha$ emission line intensity ratio, and the abundances are determined by the intensities of C VI $K\alpha$, N VI $K\alpha$, Fe XVII-L and Ne IX $K\alpha$. If we employ a multi-temperature thermal model, it may not be necessary to vary abundances because line intensity ratios can be adjusted by choosing temperatures. The most important result here is that the excess emission above the CXB below 1 keV can be represented by the emission lines of a thermal model. We tried to include additional continuum emission represented by a power-law function or thermal bremsstrahlung model. However, there was no improvement in χ^2 .

2.3. Spectral fit of “flare” spectrum

We first compared the “flare” spectrum and the best fit model for the “stable” spectrum in the 2–5 keV range. We found that there is an excess hard emission ($\chi^2/\text{d.o.f} = 46.21/16$) and added an additional power law component, as shown in figure 4. Then the “flare” 0.2–2 keV spectrum was compared with a model consisting of the best fit “stable” model and the additional power law component as shown in figure 5. The residuals at the bottom of the figure show line-like structures, so we have added nine emission lines as indicated by the arrows. All lines were modeled by delta functions of variable energy and amplitude. We show the results in the third column of table 3 and figure 6. The “flare” spectrum is well represented by the model⁴. Therefore, the enhancement of the X-ray intensity during the “flare” can be explained by an

⁴ The least significant line is that at 882 eV. By adding this line, $\chi^2/\text{d.o.f}$ was improved from 188.61/116 to 161.85/114. This line is significant at a greater than 99.98% confidence level based on the F -test.

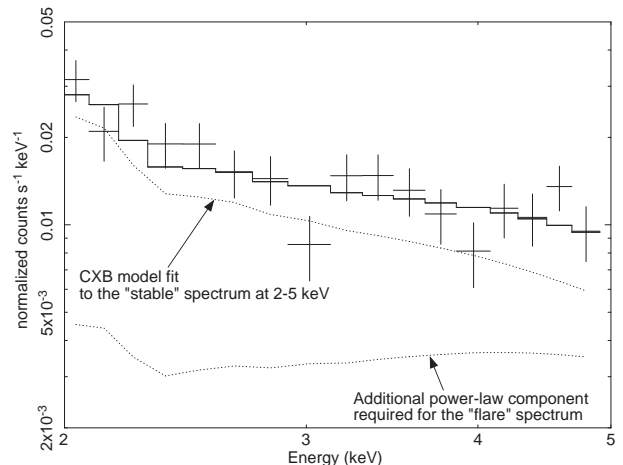


Fig. 4. Comparison of the “flare” spectrum with the CXB model fit to the “stable” spectrum at 2–5 keV. An additional power-law component was required in this range for the “flare” spectrum. Parameters are given in the second column of table 3.

increase in these emission lines and the hard power-law emission.

In the fourth column of table 3, we show probable identifications of lines. The lowest energy line below the carbon edge at 269 ± 4 eV is considered to be a sum of multiple L emission lines. The line at 455^{+5}_{-13} eV is most likely the $n = 4$ to 1 transition ($\text{Ly}\gamma$) of C VI at 459 eV, since the line energy is consistent within the statistical error and there are no other likely emission lines at this energy. If we introduced two lines at 436 eV (C VI $\text{Ly}\beta$; $n = 3$ to 1) and 459 eV (C VI $\text{Ly}\gamma$) instead of one line of variable energy, the normalizations of these lines became $1.93^{+0.75}_{-0.99}$ and

Table 3. Results of spectral fits to the “flare” spectrum. Parameter values of components added to the “stable” spectral model.

| Parameter | 2–5 keV | 0.2–2 keV | Line identification* |
|---|------------------------------------|------------------------|---|
| Additional Power-law component without absorption | | | |
| photon index Γ | 0.0 ± 1.7 | 0.0 (fixed) | |
| normalization [†] | $7.4^{+8.8}_{-1.3} \times 10^{-1}$ | 0.74 (fixed) | |
| Additional narrow Gaussian lines | | | |
| 1 | center energy [eV] — | 269 ± 4 | C band lines |
| | normalization [‡] — | $7.7^{+1.8}_{-1.7}$ | |
| 2 | center energy [eV] — | 357^{+6}_{-8} | C VI 2p to 1s (367 eV) |
| | normalization [‡] — | $7.3^{+2.2}_{-1.4}$ | |
| 3 | center energy [eV] — | 455^{+5}_{-13} | C VI 4p to 1s (459 eV) |
| | normalization [‡] — | $3.09^{+0.74}_{-0.76}$ | |
| 4 | center energy [eV] — | 558^{+8}_{-9} | O VII (561 eV) |
| | normalization [‡] — | $5.1^{+1.1}_{-1.0}$ | |
| 5 | center energy [eV] — | 649^{+4}_{-6} | O VIII 2p to 1s (653 eV) |
| | normalization [‡] — | $5.02^{+0.58}_{-0.76}$ | |
| 6 | center energy [eV] — | 796^{+10}_{-8} | Fe XVII,XVIII-L + O VIII 3p to 1s (774 eV)? |
| | normalization [‡] — | $1.67^{+0.35}_{-0.34}$ | |
| 7 | center energy [eV] — | 882^{+14}_{-17} | Fe XVII,XVIII-L + Ne IX (905 eV) |
| | normalization [‡] — | $0.95^{+0.26}_{-0.33}$ | + O VIII 6p to 1s (847 eV)? |
| 8 | center energy [eV] — | 1022^{+11}_{-7} | Ne X (1022 eV) |
| | normalization [‡] — | $1.04^{+0.20}_{-0.29}$ | |
| 9 | center energy [eV] — | 1356^{+16}_{-20} | Mg XI (1329 eV) |
| | normalization [‡] — | $0.73^{+0.19}_{-0.20}$ | |
| χ^2 /d.o.f | 17.65/14 | 161.85/114 | |

* Line energies at the rest frame are taken from Kharchenko et al. (2003), Krasnopolsky (2004). Energies of the forbidden line are shown for O VII, Ne IX, and Mg XI $K\alpha$, because the forbidden line becomes much stronger at the charge-exchange emission (e.g., Kharchenko et al. 2003).

[†] In units of photons $\text{cm}^{-2} \text{s}^{-1} \text{sr}^{-1} \text{keV}^{-1}$ at 1 keV.

[‡] In units of photons $\text{cm}^{-2} \text{s}^{-1} \text{sr}^{-1}$.

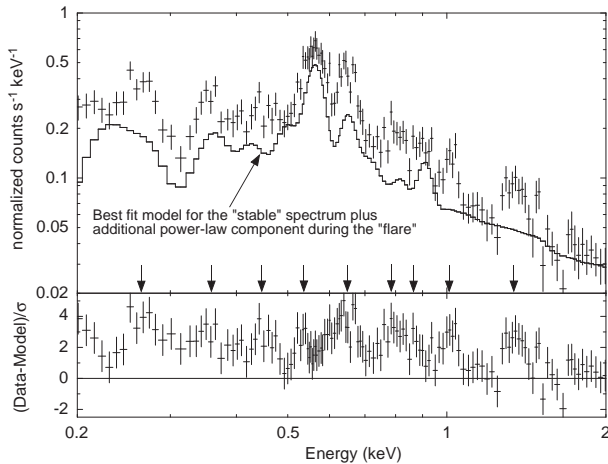


Fig. 5. Comparison of the “flare” spectrum with the best fit model for the “stable” spectrum plus additional power-law component during the “flare” in the 0.2–2 keV energy range. Vertical arrows indicate line-like structures in the residuals.

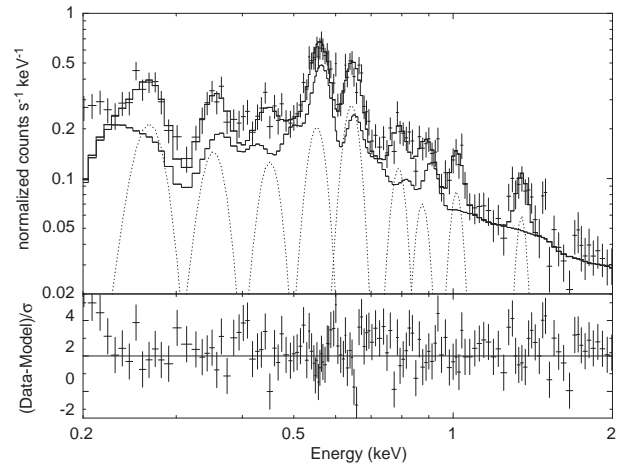


Fig. 6. “Flare” spectrum and best-fit model spectrum. The model spectrum is a sum of the best fit model for the “stable” spectrum plus additional power-law component during the “flare” shown with a thin solid curve (same as that shown in figure 5), and nine emission lines shown with dotted curves. Best-fit parameters of the nine emission lines are summarized in table 3.

$1.68_{-0.71}^{+0.76}$ photons $\text{cm}^{-2} \text{s}^{-1} \text{sr}^{-1}$, respectively. Therefore, C VI Ly β could have a comparable contribution. In either case, we definitely need the C VI Ly γ line. Dennerl et al. (2003) attributed a weak peak structure found in the XMM-Newton spectrum of comet C/2000 to a sum of C VI Ly β and Ly γ , and C VI Ly γ due to charge-exchange emission between the highly ionized solar wind and exospheric or interplanetary neutrals during an XMM-Newton observation of the Hubble Deep Field–North was reported by Snowden, Collier, Kuntz (2004). This NEP observation, however, seems to be the clearest detection so far. We also have detected O VII to Mg XI lines. The lines at 796 and 882 eV are likely to represent complex structures due to Fe-L and other lines.

3. Discussion

The short (~ 10 minutes) time scale variations observed during the enhancement of X-ray intensity imply that the size of the emission region is no larger than 10 light minutes. On the other hand, the apparent size of the emission region must be equal to or larger than the XIS field of view ($18'$). These require the emitter of the X-ray enhancement to be within a distance of 10 light minutes/ $18'$, or $\sim 10^{-3}$ pc. Because the enhanced X-ray emission consists of emission lines from C VI to Mg XI, this requires an ion source within 10^{-3} pc. There is only one ion source in this distance range. That is the Sun.

The Sun may produce X-ray emission lines in our observations in two possible ways: scattering of solar X-rays by the Earth's atmosphere, and solar-wind charge exchange. In the former case, the X-ray intensity is proportional to the solar X-ray intensity multiplied by the sunlit atmospheric column density. The solar X-ray intensity is continuously monitored by the GOES (Geostationary Operational Environmental Satellites)⁵, but data show no correlation with the enhancement. Moreover, using the MSIS atmosphere model (Hedin 1991), we found that the column density of sunlit atmosphere varied by many orders of magnitude (10^9) during the observations, but no correlation was found with the observed X-ray intensity. Thus scattering of solar X-rays can be excluded.

In figure 1, we show the proton flux observed by the ACE (Advanced Composition Explorer)⁶ together with the *Suzaku* X-ray counting rate. The ACE data were shifted in time to account for propagation time from ACE to the Earth. Clearly the proton flux was enhanced during the X-ray “flare”. This is consistent with solar-wind charge-exchange model.

Charge-exchange X-ray emission also is strongly supported by the detection of the C VI $n = 4$ to 1 transition line (Ly γ). In CIE (collisional ionization equilibrium) thermal emission, the Ly β and Ly γ lines of C VI are suppressed relative to Ly α by the Boltzmann factor in the distribution of exciting electrons. In charge exchange between C VII and H I, the electron is deposited primarily

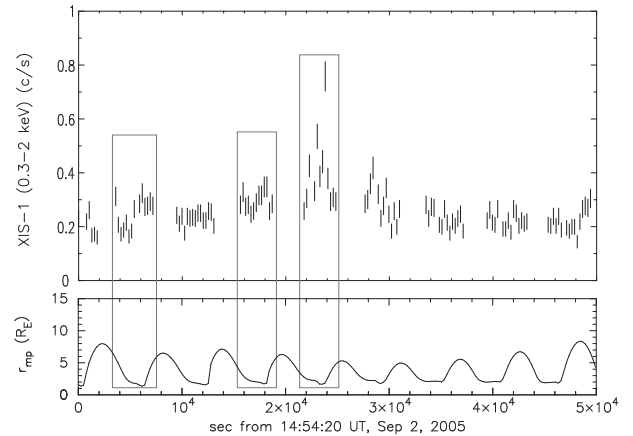


Fig. 7. 0.3–2 keV X-ray intensity (upper panel) and geocentric distance of the point whose geomagnetic field becomes open to the space for the first time along the line of sight from the spacecraft position in units of the earth radius, as a function of time during the observation (lower panel). See also the schematic view shown in figure 8.

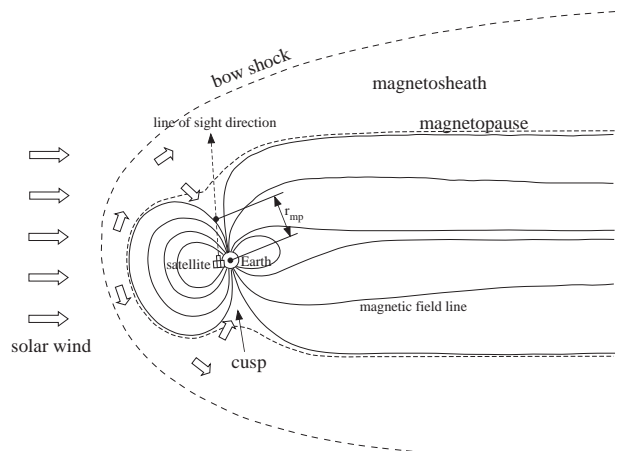


Fig. 8. Schematic view of the magnetosphere and the definition of r_{mp} used in figure 7.

in the $n = 4$ level (Krasnopolsky et al. (2004) and references therein), and the X-ray lines are produced when it cascades to the $n = 1$ level, guided only by branching ratios. In high energy collisions, angular momentum states are tend to be populated statistically by weight of the state's degeneracy, and electrons are primarily captured into maximal l , where n can change only by 1 unit at a time during the cascade (Beiersdorfer et al. 2001), again resulting in relatively weak Ly β and Ly γ . Behind the Earth's bow shock, however, the solar wind velocity is reduced, which should result in recombination into low l -orbitals and strong Ly β and Ly γ . In the “flare” spectrum, both C VI Ly α and Ly γ lines were detected and this is a strong evidence for charge exchange. In addition, O VIII $n = 3$ to 1 and $n = 6$ to 1 transition lines are also enhanced in the comet emission model (Kharchenko et al. 2003). However, we cannot separate those lines from Fe XVII-L emission lines with the present energy resolution.

⁵ The data available at <http://www.ngdc.noaa.gov/stp/GOES/goes.html>.

⁶ The data available at <http://www.srl.caltech.edu/ACE/ASC/>.

Although X-ray intensity and the proton flux are correlated on a time scale of ~ 10 hours, they do not show much correlation on short time scales. We consider that the short term X-ray intensity variation is at least partly arising from orbital motion of the spacecraft. In figure 7, we show the geocentric distance of the point whose geomagnetic field becomes open to the space for the first time along the line of sight from the spacecraft position, i.e., the point where the line of sight encounters the magnetosheath (see also the schematic view shown in figure 8 for the definition). We evaluated the end point of the magnetic field using the software GEOPACK-2005 and T96 magnetic field model (Tsyganenko, Sitnov (2005) and references therein)⁷. We obtained the solar-wind parameters required to perform the calculation from the CDAWeb (Coordinated Data Analysis Web)⁸. We find that the line of sight during the present observation was rather special in the sense that it goes through the north magnetic pole region where charged particles of the magnetosheath can penetrate down to $2-8R_{\oplus}$ moving along open field lines. The short-term X-ray intensity variations during the time intervals shown by boxes in figure 7 indicate anti-correlation with the distance to the magnetosheath. This indicates that the charge exchange of solar-wind heavy ions is taking place at $2-8R_{\oplus}$ where the neutral matter density is high. Robertson et al. (2006) recently studied theoretically solar-wind charge-exchange emission from the magnetosheath. Implications of the present results on the solar-wind ion composition and the Earth's magnetosheath including comparisons with the theoretical model will be reported in a separate paper.

Finally, since solar-wind charge-exchange emission can become a difficult foreground in the study of soft diffuse sources, we summarize a procedure to examine possible contamination in the *Suzaku* spectra below ~ 1 keV by solar activity.

1. check the light curve, if time variation is not expected for the object,
2. check the solar X-ray intensity and the column density of sunlit atmosphere along the line of sight,
3. check the solar wind proton flux,
4. check the radius of the magnetosheath on the line of sight.

We would like to thank Prof. K. Maezawa, and Prof. I. Shinohara for their help in calculations of the Earth's magnetosheath and also for valuable discussions. Thanks are also due to Prof. T. Mukai, Prof. A. Matsuoka, and Prof. H. Hayakawa for discussions on the relation between *Suzaku* data and solar wind. We are grateful to the referee, Dr. A. Dalgarno, for useful comments to improve this paper.

⁷ The software package available at <http://modelweb.gsfc.nasa.gov/magnetos/data-based/modeling.html>.

⁸ The data available at <http://cdaweb.gsfc.nasa.gov/cdaweb/sp-phys/>.

References

- Anders, E., & Grevesse, N. 1989, *Geochim. Cosmochim. Acta*, 53, 197
- Beiersdorfer, P., Lisse, C. M., Olson, R. E., Brown, G. V., & Chen, H. 2001, *ApJ*, 549, L147
- Arnaud, K. A. 1996, *ASP Conf. Ser.*, 101, 17
- Cox, D. P. 1998, *Lecture Notes in Physics* (Berlin: Springer Verlag), 506, 121
- Cravens, T. E. 2000, *ApJ*, 532, L153
- Cravens, T. E. 2002, *Science*, 296, 1042
- Dennerl, K., Englhauser, J., & Trümper, J. 1997, *Science*, 277, 1625
- Dennerl, K., Aschenbach, B., Burwitz, V., Englhauser, J., Lisse, C. M., & Rodríguez-Pascual, P. M. 2003, *SPIE*, 4851, 277
- Dickey, J. M., & Lockman, F. J. 1990, *ARA&A*, 28, 215
- Gendreau, K., et al. 1995, *PASJ*, 47, L5
- Hedin, A. E. 1991, *J. Geophys. Res.*, 96, 1159
- Ishisaki, Y. et al. 2006, submitted to *PASJ*
- Kaastra, J. S. 1992, *An X-Ray Spectral Code for Optically Thin Plasmas* (Internal SRON-Leiden Report, updated version 2.0)
- Kharchenko, V., & Dalgarno, A. 2000, *J. Geophys. Res.*, 105, 18351
- Kharchenko, V., Rigazio, M., Dalgarno, A., & Krasnopolsky, V. A. 2003, *ApJ*, 585, L73
- Koyama, K. et al. 2006, submitted to *PASJ*
- Krasnopolsky, V. A. 2004, *Icarus*, 167, 417
- Krasnopolsky, V. A., Greenwood, J. B., & Stancil, P. C. 2004, *Space Sci. Rev.*, 113, 271
- Lallement, R. 2004, *A&A*, 418, 143
- Lisse C. M., et al. 1996, *Science*, 274, 205
- Liedahl, D. A., Osterheld, A. L., & Goldstein, W. H. 1995, *ApJ*, 438, L115
- Marshall, F. E., Boldt, E. A., Holt, S. S., Miller, R. B., Mushotzky, R. F., Rose, L. A., Rothschild, R. E., & Serlemitsos, P. J. 1980, *ApJ*, 235, 4
- Mewe, R., Gronenschild, E. H. B. M., & van den Oord, G. H. J. 1985, *A&AS*, 62, 197
- Mewe, R., Lemen, J. R., & van den Oord, G. H. J. 1986, *A&AS*, 65, 511
- Mitsuda, K., et al. 2006, submitted to *PASJ*
- Pepino, R., Kharchenko, V., & Dalgarno, A. 2004, *ApJ*, 617, 1347
- Revnivtsev, M., Gilfanov, M., Jahoda, K., & Sunyaev, R. 2005, *A&A*, 444, 381
- Robertson, I. P., Cravens, T. E., Snowden, S. L., & Linde, T. 2001, *Space Sci. Rev.*, 97, 401
- Robertson, I. P., Collier, T. E., Cravens, T. E., & Fok M.-C. 2006, submitted to *J. Geophys. Res.*
- Serlemitsos, P., et al. 2006, submitted to *PASJ*
- Snowden, S. L., McCammon, D., Burrows, D. N., & Mendenhall, J. A. 1994, *ApJ*, 424, 714
- Snowden, S. L., Collier, M. R., & Kuntz, K. D. 2004, *ApJ*, 610, 1182
- Tanaka, Y., & Bleeker, J. A. M. 1977, *Space Sci. Rev.*, 20, 815
- Tsyganenko, N. A., & Sitnov, M. I. 2005, *J. Geophys. Res.*, 110, A03208, doi:10.1029/2004JA010798
- Wargelin, B. J., Markevitch, M., Juda, M., Kharchenko, V., Edgar, R., & Dalgarno, A. 2004, *ApJ*, 607, 596